ghg GREENHOUSE GASES SCIENCE AND TECHNOLOGY

Reactive fluid flow in CO_2 storage reservoirs: A 2-D pore network model study

Seunghee Kim, Western New England University, Springfield, MA, USA
J. Carlos Santamarina, King Abdullah University of Science and Technology, Thuwal, Saudi Arabia

Abstract: Water acidifies in the presence of CO_2 and prompts mineral dissolution. A 2-D pore network model scheme is developed to investigate reactive fluid flow in CO_2 storage reservoirs during injection when advective transport prevails. Mineral dissolution satisfies kinetic rate laws and continues until thermodynamic equilibrium is reached. In advection-dominant regimes, network simulation results show that species concentration, tube enlargement and flow rate can be summarized in terms of the dimensionless Damköhler number *Da* which is the ratio between advection time along a pore and the reaction time. Reservoirs will tend to experience localized enlargement near injection wells (before water drying) and compact dissolution in the far-field. The Damköhler number couples with initial pore-size variability to distort the relationship between mean tube diameter and either local or network-average flow rates. Both the Damköhler number and pore-size variability should be considered in field-scale numerical simulators. © 2015 Society of Chemical Industry and John Wiley & Sons, Ltd

Keywords: geological CO_2 storage; reactive fluid transport; pore network model; mineral dissolution; localization

Introduction

Carbon storage in geological saline aquifers has been suggested to reduce carbon emissions into the atmosphere. CO_2 enters supercritical state at temperature and pressure conditions reached when reservoir depths exceed ~800 m ($T > 304.1$K and $P >$ 7.38 MPa).[1] The solubility of supercritical CO_2 in water can reach 1~2 moles/L.[2–4] In the presence of CO_2, water with hydrogen ions H^+ and aqueous carbon dioxide $CO_{2(aq)}$ acidifies to pH~3, [5] and prompts mineral dissolution.

The evolution of reactive fluid flow depends on mineral reactivity, advection, and diffusion. Reactive fluid flow through porous media has been studied using equivalent continuum models,[6–10] single-flow channel or wormhole models,[11–13] lattice Boltzman pore-scale models,[14] and both network and discrete fracture network models.[15]

In particular, network models capture pore-scale phenomena and upscale them to predict macro-scale behavior and properties.[16] Mineral dissolution during reactive fluid flow adds complexity to network simulation, and there are only a few modeling attempts reported in the literature.[17–27] Published results show that (i) dissolution can take place uniformly across the medium, advance as a front or form wormholes depending on the ratio between advection, diffusion and reaction rates (2D);[21] (ii) the exponent of the Kozeny-Carman equation changes for different dissolution scenarios (3D);[17,20,25] and (iii) reaction rates are affected by the spatial distribution

Correspondence to: Seunghee Kim, Department of Civil and Environmental Engineering, Western New England University, 1215 Wilbraham Road, Springfield, MA 01119, USA. E-mail: simseung@gmail.com/seunghee.kim@wne.edu
Received December 10, 2013; revised September 28, 2014; accepted February 25, 2015
Published online at Wiley Online Library (wileyonlinelibrary.com). DOI: 10.1002/ghg.1487

of minerals (3D).[23,24] Network models cannot readily accommodate mechanical coupling (a study using discrete elements can be found in Shin and Santamarina[28]).

In this study, we develop a network simulation code to investigate fluid-mineral interaction when acidified water flows through a porous network. We focus on saline aquifers in carbonate formations in the context of CO_2 geologic storage.

Network simulation – preliminary concepts

Mineral dissolution – rate laws

Consider a system of interconnected pores within a calcium carbonate formation to represent minerals with fast reaction rate in saline reservoirs. The two main reactions are:[29]

$$CaCO_{3(s)} + H^+ \xrightarrow{\kappa_1} Ca^{2+} + HCO_3^- \tag{1}$$

$$CaCO_{3(s)} + CO_{2(aq)} + H_2O \xrightarrow{\kappa_2} Ca^{2+} + 2HCO_3^- \tag{2}$$

where the kinetic rate is κ [1/s] $=k_i \cdot S_s \cdot M_m$ that combines the rate constant k_i [mol/m^2/s], the mineral specific surface S_s [m^2/g] and the mineral molar mass M_m [g/ mol] (we use $S_s = 0.06$m^2/g and $M_m = 100$ g/mol for calcite).[2] The rate constants are $k_1 = 0.745$ mol/m^2/s and $k_2 = 8.6 \cdot 10^{-4}$ mol/m^2/s at a nominal temperature $T = 40$°C.[17,29–32] Assuming that the reaction rate is linearly proportional to the concentration of reactants, the rates of change in species concentrations are related as:

$$\kappa_1[H^+] = -\frac{d[H^+]}{dt} = \frac{d[Ca^{2+}]}{dt} = \frac{d[HCO_3^-]}{dt} \tag{3}$$

$$\kappa_2[H_2CO_3^*] = -\frac{d[H_2CO_3^*]}{dt} = \frac{d[Ca^{2+}]}{dt} = \frac{1}{2}\frac{d[HCO_3^-]}{dt} \tag{4}$$

where square brackets indicate species concentration and the total carbonic acid H_2CO_3* combines aqueous carbon dioxide $CO_{2(aq)}$ and carbonic acid H_2CO_3. Reactions stop when the system reaches equilibrium, and the ionic concentration product Ω equals the total equilibrium constant $K_{eq} = K_{1eq} \cdot K_{2eq}$, where $K_{1eq} = 10^{1.85}$ and $K_{2eq} = 10^{-4.5}$ are equilibrium constants for Equations 1 and 2.[17,29–32] Note that mineral precipitation is not considered in this study.

Governing parameters – simulation domain

The time scales for advection t_{adv} and diffusion t_{diff} within a channel length L_{ch}, and the chemical reaction time t_{rtn} can be combined to form two dimensionless ratios:

$$\text{Damköhler number Da} = \frac{t_{adv}}{t_{rtn}} = \frac{\kappa L_{ch}}{v_{ave}} \tag{5}$$

$$\text{Peclet number Pe} = \frac{t_{diff}}{t_{adv}} = \frac{v_{ave} L_{ch}}{D} \tag{6}$$

where v_{ave} [m/s] is the average pore velocity and D [m^2/s] is the molecular diffusion coefficient. The simulation approach is designed for advection-dominant situations where advective transport is much faster than dissolution rate ($Da << 1$); such conditions prevail in the reservoir during CO_2 injection ($Pe >> 1$).

Network construction

The 2D square network consists of tubes that intersect at nodes where incoming species mix thoroughly. Tube diameters d [m] are log-normally distributed with mean value $\overline{d_0}$ and variance *var*. All tubes have identical length L_{ch} [m]. The limitation in network size N × M is partially overcome by assuming periodic boundary conditions transverse to the flow direction. Flow is driven by the pressure difference between at inlet P_{in} and outlet P_{out} nodes (Fig. 1). The 2D network characteristics and simulation parameters are summarized in Table 1.

Numerical simulation – algorithm

General formulation

Nodal pressures and tube velocities

Nodal fluid pressures are computed by establishing fluid mass balance at all nodes, and solving the system of equations (details in Jang *et al.*[33]):

$$\sum q_i = 0 \tag{7}$$

where flow rate q [m^3/s] along each tube satisfies Poiseuille's law as a function of the tube diameter d [m], length L_{ch} [m], and the fluid viscosity μ [Pa·s]:

$$q = \frac{\Delta P \pi d^4}{128 \mu L_{ch}} \tag{8}$$

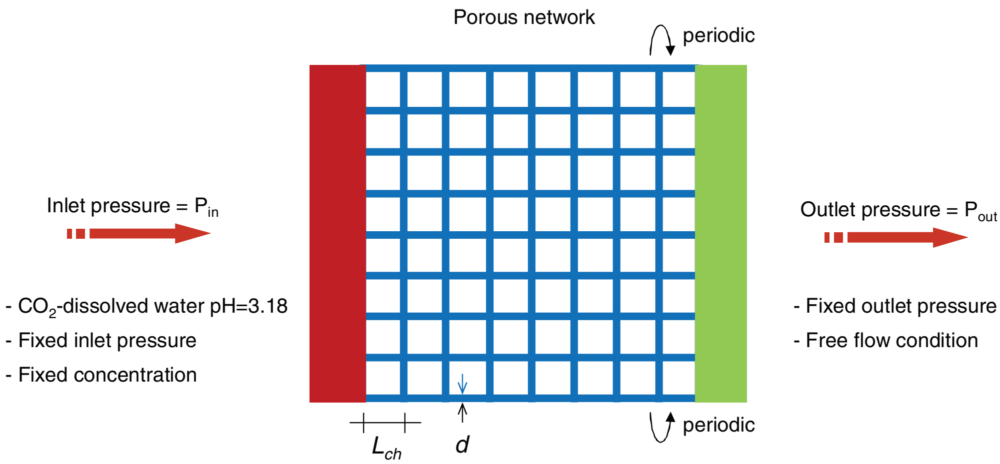

Figure 1. Pore network model: geometry, initial and boundary conditions. Fixed concentration at inlet: $[H^+] = 6.68 \times 10^{-4}$ mol/L, $[H_2CO_3^*] = 1$ mol/L, $[HCO_3^-] = 6.68 \times 10^{-4}$ mol/L, $[Ca^{2+}] = 1.361 \times 10^{-3}$ mol/L, $[OH^-] = 1.5 \times 10^{-11}$ mol/L and $[Cl^-] = 2.72 \times 10^{-3}$ mol/L.

The computed pressure difference ΔP [Pa] between two adjacent nodes is then used to compute the tube flow velocity v [m/s]:

$$v = \frac{4q}{\pi d^2} = \frac{\Delta P d^2}{32 \mu L_{ch}} \tag{9}$$

Evolution of species concentration

Mineral dissolution in a given tube lowers the concentration of reactant species and increases the concentration of produced species at the next node; this continues until the saturation concentration is reached and dissolution stops. Conditions for precipitation do not arise in this small-scale simulation (constant temperature, low pressure changes, homogeneous substrate chemistry). The concentration $c_{i+1,j+1}$ for reactant species H^+ and $H_2CO_3{}^*$ at location $x_{i+1} = x_i + \Delta x$ and time $t_{j+1} = t_j + \Delta t$ in a tube in direction x is determined by the chemical reaction rate κ, the residence time of species inside a tube L_{ch}/v, and the concentration of reactant species $c_{i,j}$ at location x_i and time t_j. For clarity, let's consider a 1D tube aligned in x; then:

$$[H^+]_{i+1,j+1} = [H^+]_{i,j} - \kappa_1 \cdot [H^+]_{i,j} \cdot \left(1 - \frac{\Omega_{i,j}}{K_{eq}}\right) \cdot \frac{L_{ch}}{v_{i,j}} \tag{10}$$

$$[H_2CO_3^*]_{i+1,j+1} = [H_2CO_3^*]_{i,j} - \kappa_2 \cdot [H_2CO_3^*]_{i,j} \cdot \left(1 - \frac{\Omega_{i,j}}{K_{eq}}\right) \cdot \frac{L_{ch}}{v_{i,j}} \tag{11}$$

where the ionic concentration product $\Omega_{i,j}$ and the velocity $v_{i,j}$ correspond to location x_i and time t_j. The concentration of produced species Ca^{2+} and $HCO_3{}^-$ are determined from the consumption of reactant species and the stoichiometric ratio between reactant and produced species. For a 1D tube aligned in x:

$$[Ca^{2+}]_{i+1,j+1} = [Ca^{2+}]_{i,j} + \left(\kappa_1 [H^+]_{i,j} + \kappa_2 [H_2CO_3^*]_{i,j}\right) \cdot \left(1 - \frac{\Omega_{i,j}}{K_{eq}}\right) \cdot \frac{L_{ch}}{v_{i,j}} \tag{12}$$

$$[HCO_3^-]_{i+1,j+1} = [HCO_3^-]_{i,j} + \left(\kappa_1 [H^+]_{i,j} + 2\kappa_2 [H_2CO_3^*]_{i,j}\right) \cdot \left(1 - \frac{\Omega_{i,j}}{K_{eq}}\right) \cdot \frac{L_{ch}}{v_{i,j}} \tag{13}$$

Table 1. Network model characteristics and simulation parameters

Entity	Property
Network size (N×M)	50 × 50
Mineralogy	Calcite
Mean of tube diameters, $\bar{d}_0$	20 μm
Distribution of tube diameters	Log-normal distribution
Coefficient of Variation, COV	0.4, 1 and 1.5
Tube length, L_{ch}	200 μm
Hydraulic gradient i_h applied at the model	10, 100 and 1000
Flushed pore volume during one cycle	$10 \cdot V_p$ (V_p: one network pore volume; $\beta = 10$)
Number of cycle (repetition)	100
Total flushed network pore volume	$1000 \cdot V_p$

These equations presume that advective transport prevails over diffusive transport ($Pe > 1$) and are valid for advection-dominant regimes.

Initial conditions

Figure 1 summarizes initial and boundary conditions. A free flux condition is assumed at outlet nodes $i = M$ in order to simulate an infinite boundary $c_{M-2,j}-c_{M-1,j} = c_{M-1,j}-c_{M,j}$. Nodes in the first column of the network ($i = 1$) define the inlet where CO_2-dissolved water is injected; these nodes have fixed concentrations of reactant species. The saturation concentration of total carbonic acid $[H_2CO_3{}^*]$ is determined using semi-empirical expressions.[5,34] Concentrations of hydrogen $[H^+]$, hydroxide $[OH^-]$, and bicarbonate $[HCO_3{}^-]$ at the inlet are obtained for a carbonate system in thermodynamic equilibrium $H_2CO_3{}^* \leftrightarrow H^+ + HCO_3{}^-$ at $T = 40°C$ and $P = 10$ MPa. Concentrations of other species, such as Ca^{2+} and Cl^- at the inlet boundary are determined to satisfy electro-neutrality. The computed initial concentrations at the inlet are (Fig. 1): $[H^+] = 6.68 \times 10^{-4}$ mol/L, $[H_2CO_3{}^*] = 1$ mol/L, $[HCO_3{}^-] = 6.68 \times 10^{-4}$ mol/L, $[Ca^{2+}] = 1.361 \times 10^{-3}$ mol/L, $[OH^-] = 1.5 \times 10^{-11}$ mol/L and $[Cl^-] = 2.72 \times 10^{-3}$ mol/L.

Chemical conditions must be initiated within the network to avoid numerical instabilities. We assume initially negligible transport of species on transverse tubes because transverse tube velocities are typically much lower than longitudinal tube velocities; once reactive flow is initiated both transverse and longitudinal transport components are taken into account. Disregarding changes in tube diameters during the early transient stage of advection, the initial 'pseudo-steady state' concentration field of reactant species along 1D longitudinal tubes can be estimated by numerically solving the differential equation for reactive fluid transport:[35]

$$\frac{dc}{dt} - v\frac{dc}{dx} - \kappa c = 0 \tag{14}$$

This equation is expressed in finite difference form (central approximation):

$$-\frac{v}{2\Delta x}\cdot c_{i+1} - \kappa\cdot c_i + \frac{v}{2\Delta x}\cdot c_{i-1} = 0 \tag{15}$$

where c_i [mol/m^3] denotes species concentration at location x_i, and the spatial interval Δx is taken as the distance between adjacent nodes $\Delta x = L_{ch}$. Note that the velocity v selected to initialize the algorithm in Eqn (15) is the average value along the longitudinal direction; thereafter, the formal 2D algorithm is applied. In matrix form,

$$\underline{\underline{A}}\cdot\underline{c} = \underline{B} \tag{16}$$

The matrix $\underline{\underline{A}}$ contains the coefficients in Equation 15 ($-v/2\Delta x$, $-\kappa$ and $v/2\Delta x$). The vector $\underline{B}$ captures boundary conditions, i.e., fixed concentration c_{inlet} at the inlet node $i = 1$ and free flux at the outlet node $i = M$. For example, the matrix $\underline{A}$ and vector $\underline{\underline{B}}$ for $M = 6$ nodes are:

$$\underline{\underline{A}} = \begin{bmatrix} 1 & 0 & 0 & 0 & 0 & 0 \\ -\frac{v}{2\Delta x} & -\kappa & \frac{v}{2\Delta x} & 0 & 0 & 0 \\ 0 & -\frac{v}{2\Delta x} & -\kappa & \frac{v}{2\Delta x} & 0 & 0 \\ 0 & 0 & -\frac{v}{2\Delta x} & -\kappa & \frac{v}{2\Delta x} & 0 \\ 0 & 0 & 0 & -\frac{v}{2\Delta x} & -\kappa & \frac{v}{2\Delta x} \\ 0 & 0 & 0 & 1 & -2 & 1 \end{bmatrix} \text{and } \underline{B} = \begin{bmatrix} c_{inlet} \\ 0 \\ 0 \\ 0 \\ 0 \\ 0 \end{bmatrix} \tag{17}$$

The sought initial pseudo-steady state concentration $\underline{c}$ of reactant species H^+ and $H_2CO_3{}^*$ at all nodes is obtained by solving the system of equations to recover the vector $\underline{c} = \underline{\underline{A}}^{-1}\cdot\underline{\underline{B}}$. The initial pseudo-steady state concentration for other species, such as Ca^{2+}, $HCO_3{}^-$, OH^-, and Cl^-, are determined to satisfy both mass balance and electro-neutrality at each node.

Complementary computations

Tube enlargement

The change in mineral concentration $\Delta c^m_{i,j}$ [mol/m^3] in the pore fluid of a tube at locations x_i and x_{i+1}, from time t_j to t_{j+1}, is computed from the consumption of reactant species H^+ and $H_2CO_3{}^*$ and their stoichiometric ratios (1:1 for both reactant species). For a 1D tube aligned in x:

$$\Delta c^m_{i,j} = \left(\kappa_1[H^+]_{i,j} + \kappa_2[H_2CO_3^*]_{i,j}\right)\cdot\left(1 - \frac{\Omega_{i,j}}{K_{eq}}\right)\cdot\frac{L_{ch}}{v_{i,j}} \tag{18}$$

The increase in tube diameter $\Delta d_{i,j}$ [m] for a tube between nodes x_i and x_{i+1} is proportional to flow rate $q_{i,j}$, the change in mineral concentration $\Delta c^m_{i,j}$, the mineral molar volume $V_m = 3.7 \times 10^{-5}$ m^3/mol (for calcite) and the elapsed time Δt [s]. For a 1D tube aligned in x:

$$\Delta d_{i,j} = \frac{2V_m\Delta t}{\pi L_{ch}}\cdot\frac{q_{i,j}}{d_{i,j}}\cdot\Delta c^m_{i,j} \tag{19}$$

The rate of mineral dissolution is much slower than the rate of advection in most problems of reactive fluid transport related to CO_2 geologic storage (Da << 1). Thus, the enlargement of tube diameters, for one replaced network pore volume V_p is minute and thus we select the time interval Δt for one iteration step to be several times β the overall advection time L_{total}/v_{ave} across the network $L_{total} = L_{ch}\cdot(M\text{-}1)$:

$$\Delta t = \beta \frac{L_{total}}{v_{ave}} \tag{20}$$

Selected β-value is listed in Table 1.

Updated nodal concentrations

The new nodal concentration $c_{i+1,j+1}{}^{new}$ for a node located at x_{i+1}, at time t_{j+1}, is computed assuming instantaneous mixing at the node:

$$c_{i+1,j+1}^{new} = \frac{\sum_k q_{k,j} \cdot c_{k+1,j+1}}{\sum_k q_{k,j}} \tag{21}$$

Algorithm

One cycle in the network simulation corresponds to the time interval Δt, and involves the following steps: (i) estimate the evolution of species concentration at the end of every tube based on species concentrations, velocity, and kinetic rates – Eqns 10 to 13, (ii) update concentration of species at all nodes – Eqn (21), (iii) compute the enlargement of tube diameter Δd for every tube – Eqns (18) to (20), and (iv) update nodal pressures, tube velocities and flow rates taking into consideration changes in tube diameters – Eqns (7) to (9). We repeat this cycle until the total flushed volume reaches 1000 pore volumes $1000\cdot V_p$ (Table 1).

Selected parameters

Reservoir pressure gradients and pore characteristics are selected to match conditions relevant to CO_2 storage reservoirs.

Distribution of Tube Diameters

The mean tube diameter $\overline{d_0}$ corresponds to typical reservoir permeabilities k_{perm} [mD] according to the following empirical expression. (Note: this expression is based on results presented in Bachu and Bennion.[36])

$$\frac{k_{perm}}{1mD} = 0.37 \cdot \left(\frac{\overline{d_0}}{1\mu m}\right)^{2.05} \tag{22}$$

We select a value $\overline{d_0}$ ≈20μm for a reservoir permeability of k_{perm}≈172 mD which is in the range for porous carbonate rocks.[20,37] Note that further analyses and results are presented in dimensionless form. Pore diameters are log-normally distributed with a coefficient of variation COV≈0.4 for most sediments;[38] we also test COV = 1.0 and 1.5 to better reflect fractured rock conditions.[39]

In situ hydraulic gradient

The hydraulic gradient is limited by the allowable injection pressure that prevents hydraulic fracture. The hydraulic gradient i_h is highest near the injection well and diminishes inversely proportional to the distance from the well. In this study, we test three different hydraulic gradients i_h = 10, 100 and 1000.

Results

Concentration

The spatial distributions of species concentrations (H^+, $H_2CO_3{}^*$, Ca^{2+} and $HCO_3{}^-$) are recorded during fluid flow (Fig. 2). When the advection time is much longer compared to the reaction time ($Da > 10^{-4}$), the concentration of reactant species (i.e., H^+ and $H_2CO_3{}^*$) rapidly decreases near the inlet. However, reactant species migrate towards the outlet as the hydraulic gradient increases and $Da<10^{-4}$. A lower consumption of reactant species accompanies high hydraulic gradients, and lower pH values are observed throughout the porous network (Fig. 3). Electro-neutrality is corroborated everywhere at all times.

Pore diameter

Tube diameter enlargement prevails near the inlet when the hydraulic gradient i_h is low i_h<100 and the Damköhler number is high $Da > 10^{-3}$ (Fig. 4(a)). More homogeneous tube enlargement is observed as the advection velocity increases (Fig. 4(b)). Figure 4 shows tube diameter enlargement after 1000 network pore volumes $1000\cdot V_p$ have been flushed. (Note: at i_h = 1000 and Da~10^{-5}, the corresponding total simulation time is two orders of magnitude longer than the characteristic time for calcite dissolution by hydrogen ions H^+.) For a given flushed volume, the higher the advection velocity the lower the eroded mass (Fig. 4(c)).

  | *Greenhouse Gas Sci Technol.* **5**:462–473 (2015); DOI: 10.1002/ghg

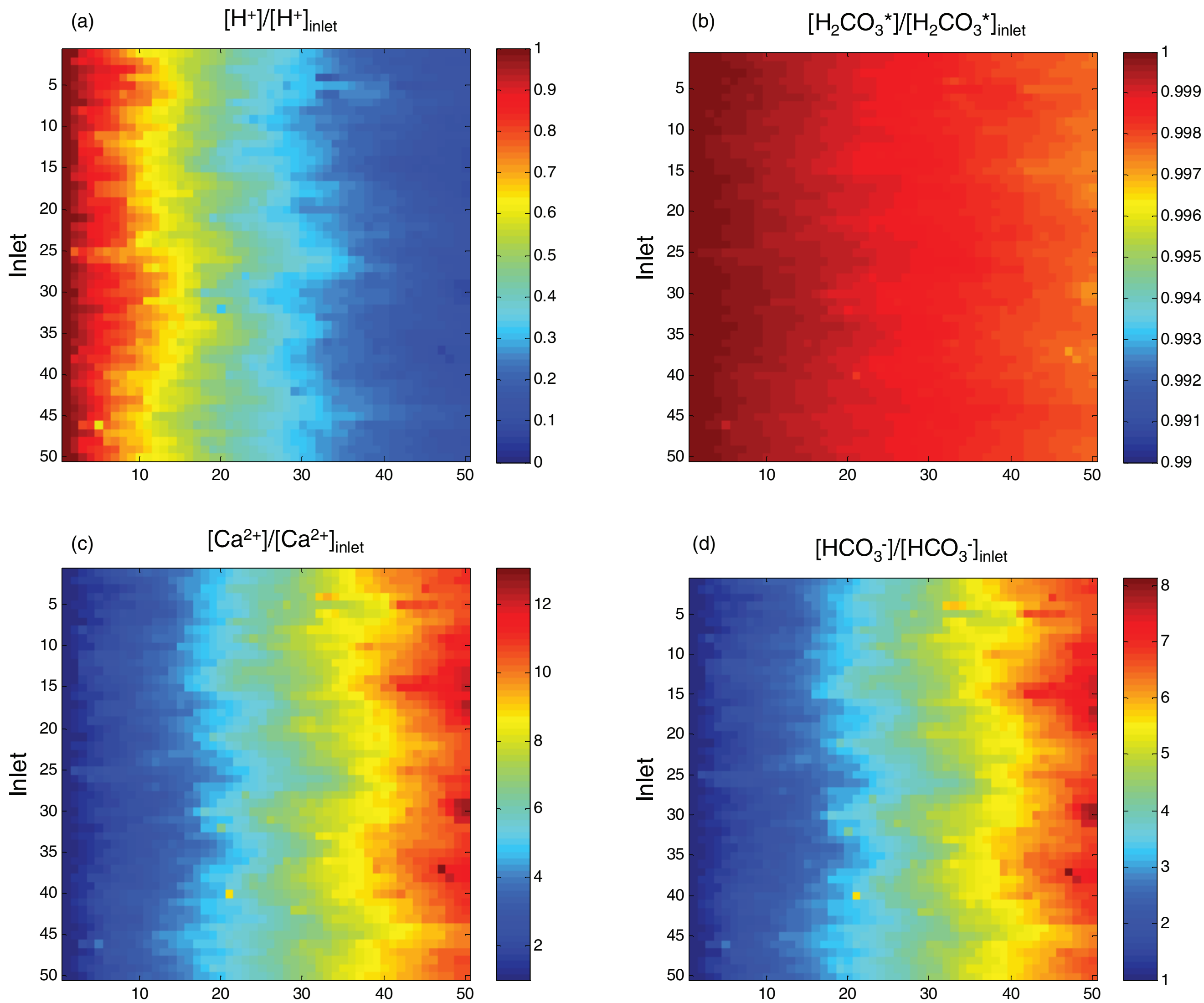

Figure 2. Distribution of species concentration after 1000 network pore volumes have been flushed through the system: (a) H^+, (b) $H_2CO_3^*$, (c) Ca^{2+} and (d) HCO_3^- (i_h = 1000, $Da = 1.5 \times 10^{-5}$ and $Pe = 6.8 \times 10^3$).

Flow rate

Reactive flow tends to preferentially enlarge tubes with initially high flow velocity as more reactants traverse the pore per unit time. This is shown in Fig. 5 where the normalized change in flow rate $\Delta q/q_{0,\max}$ is illustrated after 1000 network pore volumes for different hydraulic gradients; results are presented in terms of normalized increase in flow rate to highlight changes in the pore network and flow regime. The initial pore size distribution evolves towards localized flow and wormhole formation when $Da \leq 10^{-4}$. Conversely, flow remains relatively homogeneous after $1000 \cdot V_p$ when the hydraulic gradient is low and most reactants are consumed near the inlet (i_h = 10 and Da~10^{-3} – Fig. 5(a)).

Pressure

The pressure field in the porous medium changes with preferential tube enlargement. High dissolution at the inlet during low advection velocity brings the high inlet pressures further into the medium. As the hydraulic gradient i_h increases, dissolution extends further into the medium and the pressure field remains similar to the pre-dissolution field (Fig. 6).

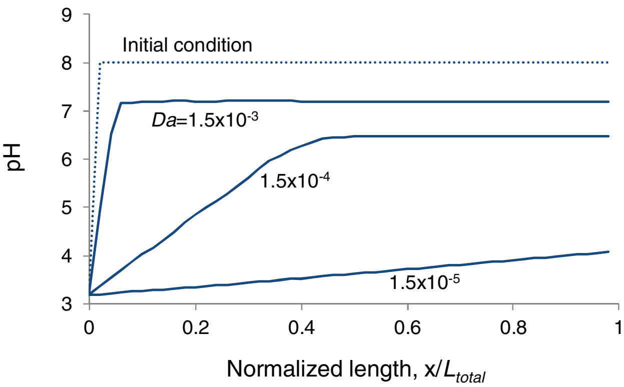

Figure 3. Evolution of pH in space and time: Average pH along the network model after 1000 network pore volumes have been flushed through the system. Note: Damköhler number decreases from $Da = 1.5 \times 10^{-3}$ to $Da = 1.5 \times 10^{-4}$ and $Da = 1.5 \times 10^{-5}$ as hydraulic gradient increases from $i_h = 10$ to $i_h = 100$ and $i_h = 1000$.

Porosity-permeability

Enlarged tube diameters mean higher porosity and permeability. The Kozeny-Carman equation suggests a power relationship between relative porosity φ/φ_0 and relative permeability k/k_0:[40]

$$\frac{k}{k_0} = \left(\frac{\varphi}{\varphi_0}\right)^{\alpha} \tag{23}$$

where φ_0 and k_0 are selected reference values. Consider a cylindrical tube in a representative elementary volume. A change in pore diameter Δd corresponds to a change in porosity $\Delta\varphi$:

$$\frac{\Delta d}{d_0} = \left(\sqrt{1+\frac{\Delta\varphi}{\varphi_0}}-1\right) \approx \frac{1}{2}\frac{\Delta\varphi}{\varphi_0} \tag{24}$$

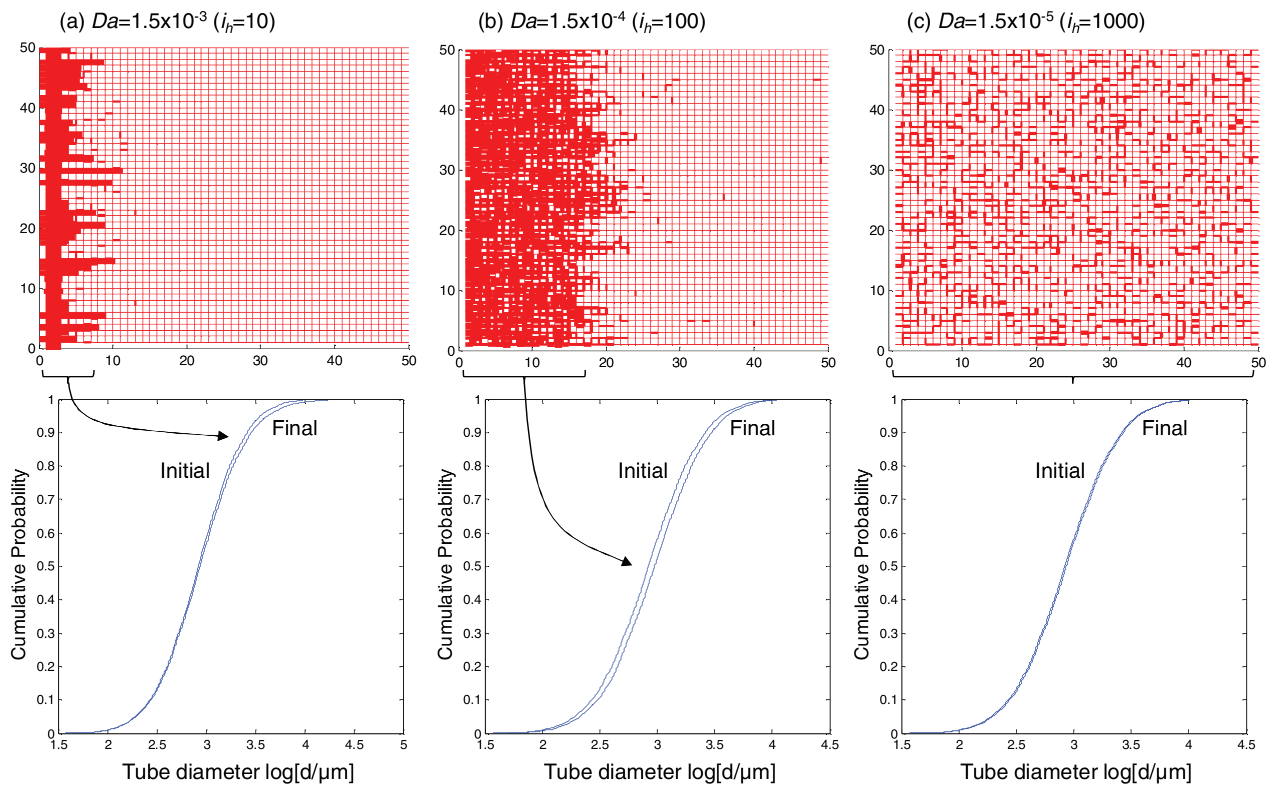

Figure 4. Evolution in tube diameters during reactive fluid transport. Cases: (a) $i_h = 10$ ($Da = 1.5 \times 10^{-3}$, $Pe = 6.8 \times 10$), (b) $i_h = 100$ ($Da = 1.5 \times 10^{-4}$, $Pe = 6.8 \times 10^2$) and (c) $i_h = 1000$ ($Da = 1.5 \times 10^{-5}$, $Pe = 6.8 \times 10^3$). Networks are drawn with line thickness proportional to the normalized increase in tube diameter ($\Delta d/d_0$). Cumulative distributions show initial tube diameters and tube diameters after 1000 network pore volumes have been flushed (coefficient of variation COV = 0.4).

where the second equality applies to small changes in normalized porosity $\Delta\varphi/\varphi_0 << 1$. Thus, changes in porosity are proportional to changes in tube diameter. Equations (23) and (24) link micro-scale changes in pore size to macro-scale changes in permeability.

  | *Greenhouse Gas Sci Technol.* **5**:462–473 (2015); DOI: 10.1002/ghg

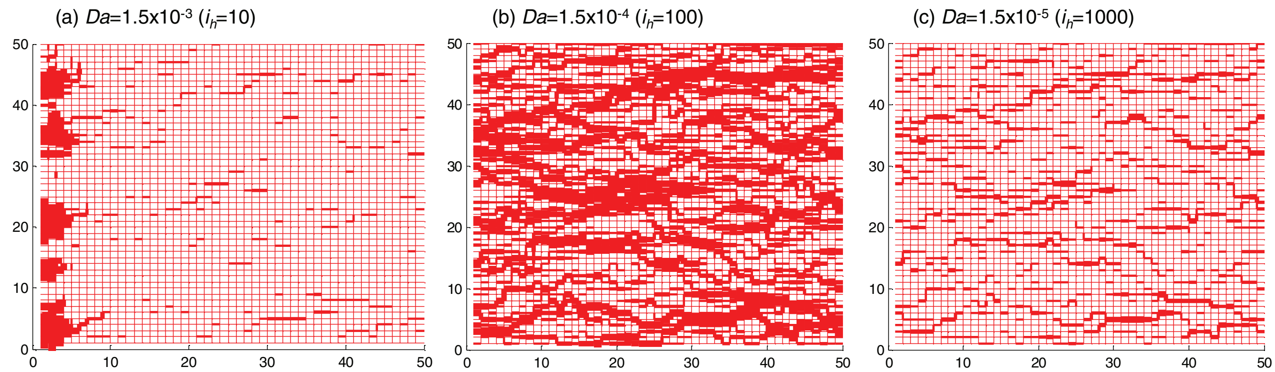

Figure 5. Evolution in flow rate across the network model. Line thickness represents normalized flow rate increase ($\Delta q/q_{0,max}$) after 1000 network pore volumes have been flushed (COV = 0.4). Cases: (a) i_h = 10 ($Da = 1.5 \times 10^{-3}$, $Pe = 6.8 \times 10$), (b) i_h = 100 ($Da = 1.5 \times 10^{-4}$, $Pe = 6.8 \times 10^2$) and (c) i_h = 1000 ($Da = 1.5 \times 10^{-5}$, $Pe = 6.8 \times 10^3$). Note: the total simulation time for $1000 \cdot V_p$ decreases from left to right. A higher mass of unconsumed reactants reaches the outlet as *Da* decreases.

When the hydraulic gradient is high $Da < 10^{-4}$ (i_h > 100), the normalized mean tube diameter $\overline{d} / \overline{d_0}$ is linearly related to the normalized flow rate q/q_0 (Fig. 7(a)). However, when the hydraulic gradient is low Da~10^{-3} (i_h = 10), the trend q/q_0 vs. $\overline{d} / \overline{d_0}$ deviates from linearity and reaches a plateau, even though the normalized mean tube diameter continues increasing; this apparent paradox is explained by the localized dissolution near the inlet (Figs (4) and (6)). Results in Fig. 7 highlight the inherent bias when network 'average' or macro-scale trends are analyzed in reactive fluid flow. While the average evolution of porosity-permeability is affected by the hydraulic gradient, *Da* and dissolution pattern in agreement with published studies,[17,20,25] these new results show deviations from the power-law relationship when individual pores and local flow rate changes are analyzed.

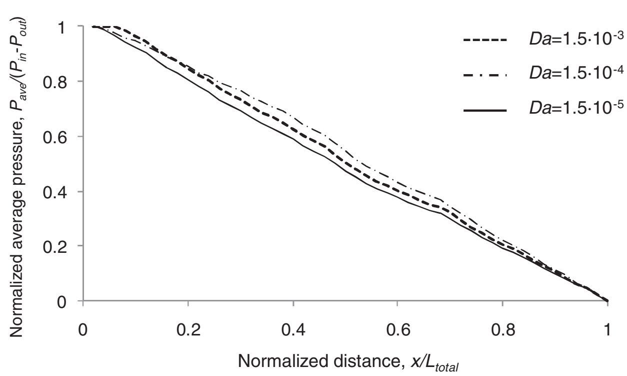

Figure 6. Normalized average pressure at distance *x* from the inlet, versus normalized distance x/L_{total} after 1000 pore volumes have been flushed through the network (Note: in all cases, the initial average pressure distribution is identical to the normalized average pressure shown for $Da = 1.5 \times 10^{-5}$).

Discussion

Dissolution pattern

We use the numerical algorithm described above to explore dissolution patterns in the context of CO_2 injection projects (Da << 1) under advection-dominant conditions (Pe >> 1). The plot in Fig. 8 summarizes all observed dissolution patterns as a function of the Damköhler number *Da*. The plot shows that water with dissolved CO_2 travelling through a carbonate system causes compact dissolution when $Da > 10^{-4}$ typically in the far field, but it localizes into a few enlarged flow channels when $Da < 10^{-4}$ typically near the inlet. These results agree with previous studies that show a transition from compact dissolution to uniform dissolution at around $10^{-4} < Da < 10^{-3}$ (injection tests of under-saturated salt solution in a porous medium made of salt grains[6]).

Initial pore-size variability

The coefficient of variation in pore size (COV) is larger in fractured rock masses than in sediments.[38,39] An additional set of simulations with COV = 1.0 and 1.5 is conducted to examine the role of pore size

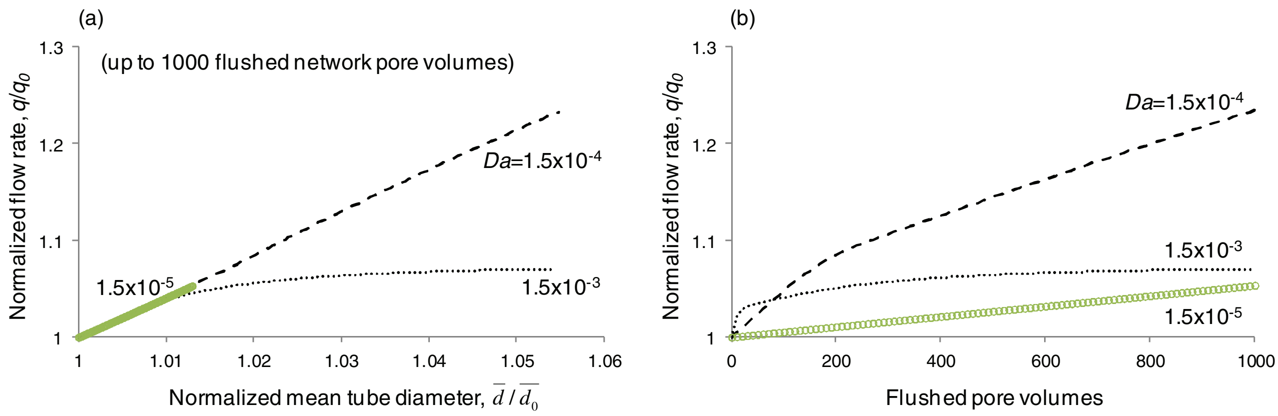

Figure 7. Evolution in flow rate normalized by the original total flow rate q/q_0 with respect to: (a) normalized mean tube diameter $\bar{d}/\bar{d}_0$, and (b) flushed pore volume for different Damköhler number *Da* (COV = 0.4). Note: Damköhler number is $Da = 1.5 \times 10^{-3}$ for hydraulic gradient $i_h = 10$, $Da = 1.5 \times 10^{-4}$ for $i_h = 100$, and $Da = 1.5 \times 10^{-5}$ for $i_h = 1000$.

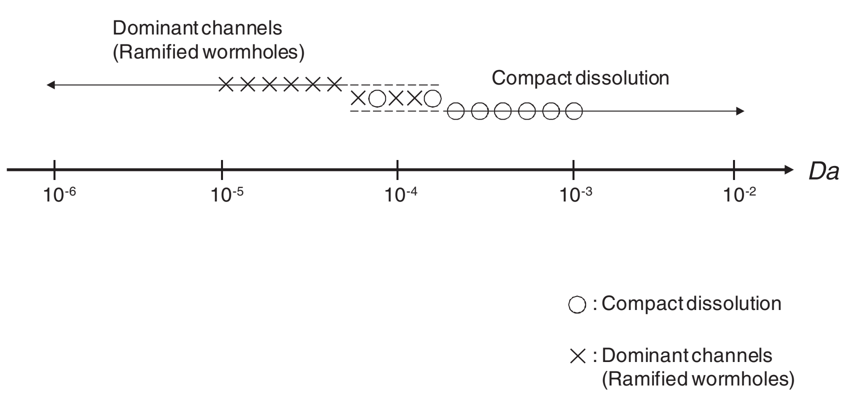

Figure 8. Dissolution pattern as a function of the Damköhler number *Da*, for 1000 flushed network pore volumes: CO_2-dissolved fluid flow through porous media during CO_2 geological storage. Note: network simulations were conducted for various hydraulic gradients $i_h = 10$ ($Da = 1.5 \times 10^{-3}$), 20-to-200 ($Da = 3 \times 10^{-4}$), and 1000 ($Da = 1.5 \times 10^{-5}$).

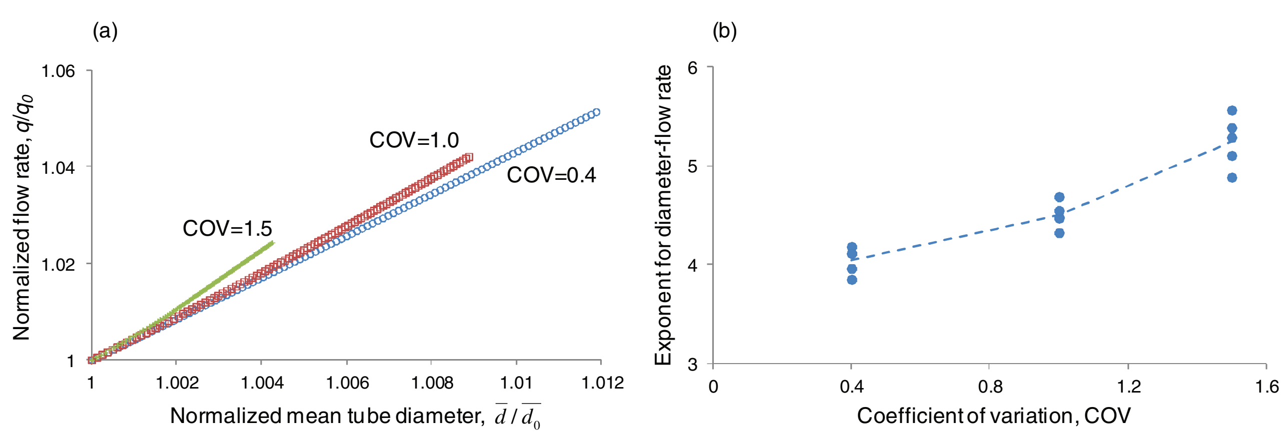

Figure 9. Flow rate and mean tube diameter evolution for different initial coefficient of variations COV in tube diameters. (a) Trends during the first 1000 network pore volumes flushed through the network under a hydraulic gradient $i_h = 1000$ ($Da = 1.5 \times 10^{-5}$). (b) Exponent α in $(q/q_o) = (\bar{d}/\bar{d}_o)^{\alpha}$ obtained for all simulations.

  | *Greenhouse Gas Sci Technol.* **5**:462–473 (2015); DOI: 10.1002/ghg

variability on the evolution of mean tube diameter and flow rate. Results in Fig. 9(a) show that the normalized flow rate increases faster with higher COV values for a given increase in the normalized mean tube diameter. Hence, the exponent for the Kozeny-Carman equation α (Eqn (23)) increases with pore-size variability. Moreover, the range in the exponent α widens as the coefficient of variation in pore size COV increases (Fig. 9(b)), in other words, a porous medium with higher pore size variability COV will experience higher flow localization and fewer channels will carry most of the flow.

Conclusions

Reactive fluid flow is triggered at the CO_2-water interface, where CO_2 dissolves into water and travels into the reservoir. Pore network simulation results show:

- In advection-dominant regimes, species concentration, tube enlargement and flow rate can be summarized in terms of the dimensionless Damköhler number *Da* which is the ratio between advection time along a pore and the reaction time.
- The concentration of reactant species rapidly decreases near the inlet when the pressure gradient is low and Damköhler number exceeds $Da > 10^{-4}$. In this case, tube diameter enlargement prevails near the inlet and advances homogeneously into the formation; hence, the high inlet pressure is gradually transferred further into the formation.
- Reactant species migrate towards the outlet and ramify as the pressure gradient increases and the Damköhler number drops below $Da < 10^{-4}$. Tube enlargement is observed throughout the network at high advection velocities; however, channels with initially high flow rate experience most of the increase in flow rate.
- Calcite storage reservoirs will experience compact dissolution in the far field when $Da > 10^{-4}$ and localized dissolution when $Da < 10^{-4}$ (before drying) as a result of CO_2-dissolved reactive fluid flow.
- The Damköhler number couples with initial pore-size variability to distort the relationship between mean tube diameter and flow rate. In particular, the relationship can be significantly different when 'network average' values are considered for reservoir analysis, and the exponent of the Kozeny-Carman equation $q/q_0 = (\varphi/\varphi_0)^\alpha$ increases with the coefficient of variation COV in pore size. Therefore, both the Damköhler number and pore-size variability should be considered in field-scale numerical simulators.

Acknowledgements

Support for this research was provided by the US Department of Energy project DE-FE0001826. Any opinion, findings, conclusions, or recommendations expressed herein are those of the authors and do not necessarily reflect the views of funding organizations. F. J. Santamarina carefully edited this manuscript. This research was conducted while the authors were at Georgia Institute of Technology.

References

1. Span R and Wagner W, A new equation of state for carbon dioxide covering the fluid region from the triple point temperature to 1,100 K at pressures up to 800 MPa. *J Phys Chem Ref Data* **25**(6):1509–1596 (1996).
2. Gaus I, Azaroual M and Czernichowski-Lauriol I, Reactive transport modelling of the impact of CO_2 injection on the clayey cap rock at Sleipner (North Sea). *Chem Geol* **217**(3/4):319–337 (2005).
3. Kharaka YK, Cole DR, Hovorka SD, Gunter WD, Knauss KG and Freifeld BM, Gas-water-rock interactions in Frio formation following CO_2 injection: Implications for the storage of greenhouse gases in sedimentary basins. *Geology* **34**(7):577–580 (2006).
4. White DJ, Burrowes G, Davis T, Hajnal Z, Hirsche K, Hutcheon I et al., Greenhouse gas sequestration in abandoned oil reservoirs: The International Energy Agency Weyburn pilot project. *GSA Today* **14**(7):4–10 (2004).
5. Kim S, *CO_2 Geological Storage: Hydro-Chemo-Mechanically Coupled Phenomena and Engineered Injection*. Georgia Institute of Technology, Atlanta (2012).
6. Golfier F, Zarcone C, Bazin B, Lenormand R, Lasseux D and Quintard M, On the ability of a Darcy-scale model to capture wormhole formation during the dissolution of a porous medium. *J Fluid Mech* **457**(213):213–254 (2002).
7. Kalia N and Balakotaiah V, Modeling and analysis of wormhole formation in reactive dissolution of carbonate rocks. *Chem Eng Sci* **62**(4):919–928 (2007).
8. Liu X, Ormond A, Bartko K, Ying L and Ortoleva P, A geochemical reaction-transport simulator for matrix acidizing analysis and design. *J Petrol Sci Eng* **17**(1/2):181–196 (1997).
9. Panga MKR, Ziauddin M and Balakotaiah V, Two scale continuum model for simulation of wormholes in carbonate acidization. *AIChE J* **51**(12):3231–3248 (2005).
10. Xu T, Sonnenthal E, Spycher N and Pruess K, TOUGHREACT–A simulation program for non-isothermal multiphase reactive geochemical transport in variably saturated geologic media: Applications to geothermal injectivity and CO_2 geological sequestration. *Comput Geosci* **32**(2):145–165 (2006).

11. Buijse M, Understanding wormholing mechanisms can improve acid treatments in carbonate formations. *Old Prod Facil* **15**(3):168–175 (2000).
12. Hung KM, Hill AD and Sepehrnoori K, A mechanistic model of wormhole growth in carbonate matrix acidizing and acid fracturing. *J Petrol Technol* **41**(1):59–66 (1989).
13. Li L, Steefel CI and Yang L, Scale dependence of mineral dissolution rates within single pores and fractures. *Geochim Cosmochim Acta* **72**(2):360–377 (2008).
14. Kang Q, Lichtner PC, Viswanathan HS and Abdel-Fattah AI, Pore scale modeling of reactive transport involved in geologic CO_2 sequestration. *Trans Porous Med* **82**(1):197–213 (2010).
15. Steefel CI, DePaolo DJ and Lichtner PC, Reactive transport modeling: An essential tool and a new research approach for the Earth sciences. *Earth Planet Sci Lett* **240**(3/4):539–558 (2005).
16. Dillard LA and Blunt MJ, Development of a pore network simulation model to study nonaqueous phase liquid dissolution. *Water Resource Res* **36**(2):439–454 (2000).
17. AlgiveL , BekriS and Vizika-kavvadiasO (eds), Reactive pore network modeling dedicated to the determination of the petrophysical property changes while injecting CO_2, in *SPE Annual Technical Conference and Exhibition,* 4–7 October. Society of Petroleum Engineers, New Orleans, Louisiana, USA. (2009).
18. Daccord G, Lenormand R and Lietard O, Chemical dissolution of a porous-medium by a reactive fluid. 1. Model for the wormholing phenomenon. *Chem Eng Sci* **48**(1):169–178 (1993).
19. Daccord G, Lietard O and Lenormand R, Chemical dissolution of a porous-medium by a reactive fluid. 2. Convection vs. reaction, behavior diagram. *Chem Eng Sci* **48**(1):179–186 (1993).
20. Egermann P, Bekri S and Vizika O, An integrated approach to assess the petrophysical properties of rocks altered by rock/fluid interactions (CO_2 injection). *Petrophysics* **51**(1):32–40 (2010).
21. Fredd CN and Fogler HS, Influence of transport and reaction on wormhole formation in porous media. *AIChE J* **44**(9):1933–1949 (1998).
22. Hoefner ML and Fogler HS, Pore evolution and channel formation during flow and reaction in porous media. *AIChE J* **34**(1):45–54 (1988).
23. Li L, Peters CA and Celia MA, Upscaling geochemical reaction rates using pore-scale network modeling. *Adv Water Resource* **29**(9):1351–1370 (2006).
24. Li L, Peters CA and Celia MA, Effects of mineral spatial distribution on reaction rates in porous media. *Water Resource Res* **43**(1):W01419 (2007).
25. Nogues JP, Fitts JP, Celia MA and Peters CA, Permeability evolution due to dissolution and precipitation of carbonates using reactive transport modeling in pore networks. *Water Resource Res* **49**(9):6006–6021 (2013).
26. Raoof A, Nick H, Hassanizadeh S and Spiers C, PoreFlow: A complex pore-network model for simulation of reactive transport in variably saturated porous media. *Comput Geosci* **61**:160–174 (2013).
27. Varloteaux C, Vu MT, Békri S and Adler PM, Reactive transport in porous media: Pore-network model approach compared to pore-scale model. *Phys Rev E* **87**(2):023010 (2013).
28. Shin H and Santamarina JC, Mineral dissolution and the evolution of k_0. *J Geotech Geoenviron* **135**(8):1141–1147 (2009).
29. Plummer LN, Wigley TML and Parkhurst DL, The kinetics of calcite dissolution in CO_2-water systems at 5 to 60 degC and 0.0 to 1.0 atm CO_2. *Am J Sci* **278**(2):179–216 (1978).
30. Fredd CN and Fogler HS, The kinetics of calcite dissolution in acetic acid solutions. *Chem Eng Sci* **53**(22):3863–3874 (1998).
31. Pokrovsky OS, Golubev SV and Schott J, Dissolution kinetics of calcite, dolomite and magnesite at 25 C and 0 to 50 atm pCO_2. *Chem Geol* **217**(3/4):239–255 (2005).
32. Renard F, Gundersen E, Hellmann R, Collombet M and Le Guen Y, Numerical modeling of the effect of carbon dioxide sequestration on the rate of pressure solution creep in limestone: Preliminary results. *Oil Gas Sci Technol* **60**(2):381–399 (2005).
33. Jang J, Narsilio GA and Santamarina JC, Hydraulic conductivity in spatially varying media – a pore scale investigation. *Geophys J Int* **184**(3):1167–1179 (2011).
34. Duan Z and Sun R, An improved model calculating CO_2 solubility in pure water and aqueous NaCl solutions from 273 to 533 K and from 0 to 2000 bar. *Chem Geol* **193**(3/4):257–271 (2003).
35. Boudreau BP, *Diagenetic models and their implementation: Modelling transport and reactions in aquatic sediments*. Springer, Berlin (1997).
36. Bachu S and Bennion B, Effects of in-situ conditions on relative permeability characteristics of CO_2-brine systems. *Environ Geol* **54**(8):1707–1722 (2008).
37. Brosse E, Magnier C and Vincent B, Modelling fluid-rock interaction induced by the percolation of CO_2-enriched solutions in core samples: The role of reactive surface area. *Oil Gas Sci Technol* **60**(2):287–305 (2005).
38. Phadnis HS and Santamarina JC, Bacteria in sediments: Pore size effects. *Geotech Lett* **1**:91–93 (2011).
39. Wellman TP, Shapiro AM and Hill MC, Effects of simplifying fracture network representation on inert chemical migration in fracture-controlled aquifers. *Water Resource Res* **45**:W01416 (2009).
40. Carman PC, *Flow of Gases through Porous Media*. Butterworths, London (1956).

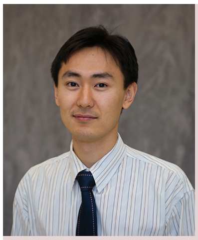

Seunghee Kim

Seunghee Kim is an Assistant Professor of Civil and Environmental Engineering at Western New England University. He received a Ph.D. in Civil and Environmental Engineering from the Georgia Institute of Technology, and conducted a postdoctoral study at the Bureau of Economic Geology, the University of Texas at Austin. His current research interests include hydro-chemo-thermo-mechanically coupled processes for energy-related situations such as CO_2 sequestration, underground storage, and geothermal energy.

J. Carlos Santamarina

J. Carlos Santamarina is a Professor of Earth Science and Engineering at the King Abdullah University of Science and Technology (KAUST). His research team explores the scientific foundations of geomaterial behavior and subsurface processes using particle-level and pore-scale experiments, combined with numerical methods and high-resolution process monitoring systems.